AIAA 2016-0586
AIAA SciTech
4-8 January 2016, San Diego, California, USA
54th AIAA Aerospace Sciences Meeting

Development and Validation of a LES Turbulence Wall Model for Compressible Flows with Heat Transfer

Jeffrey R. Komives*
Aerospace Engineering and Mechanics
University of Minnesota, Minneapolis, MN, 55455

Pramod K. Subbareddy†
Mechanical and Aerospace Engineering
North Carolina State University, Raleigh, NC, 27695

Graham V. Candler‡
Aerospace Engineering and Mechanics
University of Minnesota, Minneapolis, MN, 55455

The numerical simulation of turbulent hypersonic flows poses a number of significant challenges. Chief among these challenges is the stringent grid resolution requirement in the boundary layer to accurately predict wall heat flux and skin friction. An enabling modeling concept for such flows is the use of wall models to reduce the near wall computational burden. In this paper, we present the development and validation of a turbulence wall model applicable to high Reynolds number flows. We review modeling choices that arise given a use case of cold-wall hypersonic flow with shock-turbulent boundary layer interaction. Finally, we assess the performance of the model in an a posteriori analysis of a hollow cylinder-flare forebody and a large cone-flare forebody, and comment on model performance and limitations.

Nomenclature

h_{wm}	wall model probe height
$F,\ G$	flux vector
N	number of point/elements
Q	vector of solution variables
q	heat flux
Re	Reynolds Number
U	vector of conserved variables
u, v, w	velocity
x, y, z	displacement or position
Δ	difference operator
δ	update
κ	von Karman constant, thermal conductivity
$\tilde{\nu}$	Spalart-Allmaras variable
τ	shear

Superscript

k	iteration
n	time-level of simulation
$+$	wall-units

Subscript

$1, 2, 3$	coordinate directions in wall-frame
j	index of summation
t	turbulent
w	wall

*PhD Candidate, Member AIAA.
†Assistant Professor, Member AIAA
‡Russell J. Penrose and McKnight Presidential Professor, Fellow AIAA
The views expressed in this article are those of the author and do not reflect the official policy or position of the United States Air Force, Department of Defense, or the U.S. Government.

I. Introduction

Turbulence models for Reynolds-Averaged Navier-Stokes (RANS) and Wall-Resolved Large Eddy Simulations (WR-LES) have stringent grid resolution requirements near solid boundaries to produce accurate boundary layers and surface quantities. A typical requirement is that the maximum height of the wall-adjacent cell across the entire boundary be kept under one in wall units ($y^+ \leq 1$). This requirement dictates that a large percentage of the cells used in a given calculation be allocated to the boundary layer, limiting the maximum Reynolds number that can be achieved on a given computational resource. Additionally, the small dimensions of the cells near the wall give rise to restrictive timestep limitations. In order to rapidly converge high Reynolds number flows of engineering interest, an alternative solution strategy is required.

Recently, Choi and Moin[1] have revisited Chapman's[2] classic scaling estimates using a more current understanding of how skin friction scales at high Reynolds number. Using this revised data, grid requirements for high Reynolds number simulations scale with Reynolds number as shown in table 1. In order to compute high Reynolds number flows of engineering interest, wall-resolved LES is not a feasible solution as the grid requirements are nearly quadratic with Reynolds number.

Direct Numerical Simulation	$N \sim \mathrm{Re}^{37/14}$
Wall-Resolved LES	$N \sim \mathrm{Re}^{13/7}$
Wall-Modeled LES	$N \sim \mathrm{Re}$

Table 1. Grid requirements for high Reynolds number turbulent boundary layers, from Choi and Moin.[1]

A preponderance of the existing literature on wall models for high Reynolds number flows assume that the turbulent boundary layer experiences a zero or mild pressure gradient, and that all inertial terms balance.[3–6] Under these assumptions, conservation of streamwise momentum reduces to a simple expression of constant shear ($\mu \frac{\mathrm{d}u}{\mathrm{d}y} = \mathrm{const}$), which is appealing due to the straightforward solution procedure required for the ODE, and the availability of analytic solutions in the form of the well known law of the wall.[7] Fewer works attempt to model heat transfer within the wall model framework, but those that do often assume adiabatic walls and flows with mild density gradients.

To overcome the wall spacing restriction inherent to high Reynolds number RANS or WR-RES, we have developed a wall model that predicts surface quantities and boundary layer profiles on under-resolved grids ($y^+ \gg 1$). Particular attention was placed to ensure that the derivation of the model is valid for high Reynolds number flows in the hypersonic regime, including regions of Shock Turbulent Boundary Layer Interaction (STBLI). Model derivation, performance and limitations are discussed. Simulations thus far were run a posteriori using converged solutions from the University of Minnesota hypersonics research code, US3D.[8]

II. Recent Efforts

Several researchers in recent years have examined the accuracy of different wall model formulations for application in WM-LES in various flow regimes. Kawai and Larsson[3] examined the standard practice in WM-LES of using data from the wall-adjacent computational cell in the LES as the boundary condition for a wall model. They show that WM-LES calculations are necessarily under resolved in the wall-adjacent cell, and that the use of such cells in a wall model will introduce numerical error. Instead, the authors propose sampling data for the wall model from a position a few cells into the computational domain, approximately in the log-layer for an equilibrium boundary layer. They show very favorable results on a compressible flat plate with using an interrogation location placed a few cells into the boundary layer. One important implication of this method is that the interrogation location of their wall model is placed significantly further into the boundary layer than a method that uses the wall-adjacent cell as the interrogation location.

Dawson, Bodart and Lele[4] developed a wall model inspired by Kawai and Larsson[3] to examine STBLI in the form of a compression ramp. A refined mesh is embedded into the coarse LES mesh, and the equilibrium boundary layer equations are solved (temperature dependent). In an equilibrium model, all terms of the Navier-Stokes equations are assumed to be negligible with the exception of the wall-normal viscous shear term. They use the wall shear and heat transfer results of the wall model calculations as boundary conditions for the LES. In their paper, Dawson et al., clearly make the case that equilibrium models are insufficient to model compression ramps or other STBLI flows involving separation. They show that the assumption of neglecting pressure and convective terms of the streamwise-momentum equation, while appropriate for a flat plate, neglect important physics involved in the STBLI.

Hickel, Touber, Bodart and Larsson[9] developed a zonal method that includes non-equilibrium effects while retaining connectivity in only the wall-normal direction. Importantly, they showed that retaining the pressure gradient term while neglecting convection terms resulted in momentum not being balanced in a control volume away from the wall. The inclusion of both terms is necessary to capture non-equilibrium effects. Their model parameterizes the convective term in the boundary layer equation based on either the streamwise pressure gradient in the outer layer or the mean streamwise convective term in the outer layer. When applying this model to a wall-resolved dataset in an a posteriori analysis, the pressure gradient method proved to be more robust and accurate than the second method, however neither led to a more accurate prediction of skin friction than an equilibrium model.

III. Model Development

The primary error caused by under-resolved wall cells is an incorrect viscous flux calculation due to inaccurate gradients evaluated at the wall. The purpose of a wall model is to leverage knowledge of the physics of turbulent boundary layers to correct the calculation of wall shear and heat transfer to a physically meaningful value. As discussed in section II, an equilibrium wall model will not be accurate for STBLI flows with heat transfer due to the omission of pressure-gradient, convection and compressibility effects. We have developed a wall-model that retains the necessary physics to resolve STBLI flows. The model is summarized as follows.

A reduced set of the Reynolds Averaged Navier Stokes equations are solved in the modeled region. This is necessary to account for compressibility, heat transfer and inertial effects. Input data for the model is sampled several cells away from the wall. This places the interface location with the parent calculation, or probe point, in the log-layer and avoids unresolved data in the wall-adjacent cells. A schematic of the embedded wall grid within the LES grid is shown in Fig. 1. The model equations are solved via a 1-D iterative method on a virtual grid embedded within the LES. While the iterative method is coupled in the wall-normal direction, connectivity is used between the wall-normal solves to allow us to evaluate the convective terms of the Navier-Stokes equations. We believe that these terms, often ignored in wall modeling, are necessary in non-equilibrium STBLI flows. The wall model solution at the boundary is then used by the LES to inform the construction of viscous fluxes at the wall.

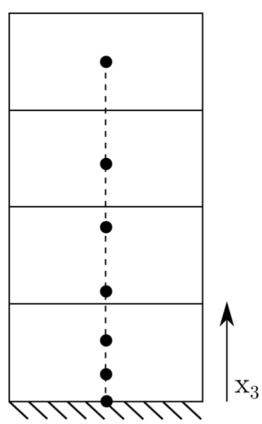

Figure 1. Schematic of wall grid shown within LES grid.

III.A. Governing Equations

We start by defining a wall-based coordinate system where x_1 and x_2 are two arbitrary, orthogonal wall-tangent directions and x_3 is the wall-normal. The Navier-Stokes equations in divergence form are:

$$\frac{\partial U}{\partial t} + \frac{\partial F_1}{\partial x_1} + \frac{\partial F_2}{\partial x_2} + \frac{\partial F_3}{\partial x_3} = 0 \tag{1}$$

where U and F_j are the vectors of conserved variables and fluxes respectively.

$$U = \begin{pmatrix} \rho \\ \rho u_1 \\ \rho u_2 \\ \rho u_3 \\ E \end{pmatrix}, \quad F_j = \begin{pmatrix} \rho u_j \\ \rho u_1 u_j + p\delta_{1j} - \sigma_{1j} \\ \rho u_2 u_j + p\delta_{2j} - \sigma_{2j} \\ \rho u_3 u_j + p\delta_{3j} - \sigma_{3j} \\ (E+p)u_j - \sigma_{kj}u_k - q_j \end{pmatrix} \tag{2}$$

The viscous stress tensor, σ_{ij}, and heat conduction vector, q_j, are defined as

$$\sigma_{ij} = \hat{\mu}\left(\frac{\partial u_i}{\partial x_j} + \frac{\partial u_j}{\partial x_i}\right) - \frac{2}{3}\hat{\mu}\frac{\partial u_k}{\partial x_k}\delta_{ij} \tag{3}$$

$$q_j = \hat{\kappa}\frac{\partial T}{\partial x_j} \tag{4}$$

where the effective viscosity and thermal conductivity are approximated via the Boussinesq approximation as the sum of a molecular and turbulent component

$$\hat{\mu} = \mu + \mu_t, \qquad \hat{\kappa} = \kappa + \kappa_t \tag{5}$$

We assume the pressure to be constant in the wall-normal direction, which allows us to decouple conservation of wall-normal momentum and conservation of mass from the equation set. For an perfect gas, the equation of state allows us to recover the density field solely from the temperature field for an isobaric gas.

$$\rho_i = \frac{P_e}{RT_i} \tag{6}$$

As suggested by the solution strategy of Bond and Blottner,[10] the density field and flow primitives can be updated in an outer loop while each of the remaining governing equations are solved in a decoupled fashion in an inner loop. Assuming no time-derivative of density, we recast the above equations as:

$$\frac{\partial Q}{\partial t} + \frac{1}{\rho}\left[\frac{\partial G_1}{\partial x_1} + \frac{\partial G_2}{\partial x_2} + \frac{\partial G_3}{\partial x_3}\right] = 0 \tag{7}$$

where Q is the solution vector with density decoupled, and G_j is the flux vector of the reduced set of equations.

$$Q = \begin{pmatrix} u_1 \\ u_2 \\ e \end{pmatrix}, \quad G_j = \begin{pmatrix} \rho u_1 u_j + p\delta_{1j} - \sigma_{1j} \\ \rho u_2 u_j + p\delta_{2j} - \sigma_{2j} \\ (E+p)u_j - \sigma_{kj}u_k - q_j \end{pmatrix} \tag{8}$$

The equation for conservation of wall normal momentum is not necessary since under the boundary-layer assumptions it reduces to the invariance of pressure in the wall normal direction ($\frac{\partial P}{\partial x_3} = 0$). Constant pressure in the boundary layer then allows us to decouple conservation of mass and prescribe density from an equation of state. The equations are expressed in terms of the primitives to decouple the density field, which has severe changes in gradient, from the ODEs being solved. The resulting velocities and specific energy fields are monotonic and better conditioned for implicit solution.

These equations are discretized on an embedded node-based mesh in the near wall region. The outermost node coincides with the probe location in the solver, and the innermost node is on the wall face.

III.B. Eddy Viscosity Modeling

This paper will examine the performance of two different eddy viscosity models in the proposed wall model. The first model examined is a simple mixing length model with near-wall damping. This type of model is the one most typically found in compressible wall models.[3,4,6,11,12]

$$D = \left[1 - e^{-(x_3^\star / A^+)}\right]^2 \tag{9}$$

$$\mu_t = \rho \kappa x_3 \sqrt{\frac{\tau_w}{\rho}} D \tag{10}$$

where $A^+ = 17$ and the von Karman constant is chosen as $\kappa = 0.41$. The wall coordinate used in the damping function, D, is modified to account for cold wall conditions.

$$x_3^\star = x_3 \frac{\sqrt{\rho \tau_w}}{\mu} \tag{11}$$

The second model chosen for this work is the compressible form of the Spalart-Allmaras turbulence model proposed by Catris and Aupoix[13] (SA-Catris). This eddy viscosity model is very similar to the formulation of the SA model used by Bond and Blottner[10] in their study. Using the assumptions inherited so far in this work and only considering gradients in the wall-normal direction, the SA-Catris model is expressed as:

$$\frac{\partial \tilde{\nu}}{\partial t} = \frac{1}{\rho}(S_P - S_D + D) \tag{12}$$

where

$$S_P = c_{b1} \tilde{S} \rho \tilde{\nu} \tag{13}$$

$$S_D = c_{w1} f_w \rho \left(\frac{\tilde{\nu}}{d}\right)^2 \tag{14}$$

$$D = \frac{1}{\sigma}\left[\frac{\partial}{\partial x_3}\left(\mu \frac{\partial \tilde{\nu}}{\partial x_3}\right) + \frac{\partial}{\partial x_3}\left(\sqrt{\rho}\tilde{\nu} \frac{\partial \sqrt{\rho}\tilde{\nu}}{\partial x_3}\right) + c_{b2} \frac{\partial \sqrt{\rho}\tilde{\nu}}{\partial x_3} \frac{\partial \sqrt{\rho}\tilde{\nu}}{\partial x_3}\right] \tag{15}$$

Equation (12) is added to the set solved in Eq. (7). The model coefficients in Eqs. (13) - (15) are taken from the standard SA model. The turbulent Prandtl number for all models is chosen to be a constant 0.9.

III.C. Solution Form

Given the strong coupling in the wall-normal direction, the flux-derivatives in the wall-tangent directions can be evaluated explicitly and moved to the right-hand side.

$$\left.\frac{\partial Q}{\partial t}\right|^{n+1} + \frac{1}{\rho}\left.\frac{\partial G_3}{\partial x_3}\right|^{n+1} = -\frac{1}{\rho}\sum_{j=1}^{2}\left.\frac{\partial G_j}{\partial x_j}\right|^{n} \tag{16}$$

The terms on the left-hand side of Eq (16) (including the SA-Catris equation) are cast into delta-form yielding a set of tri-diagonal scalar systems that are solved iteratively until convergence.

A number of other assumptions simplify the numerical procedure. Namely, viscous fluxes in the x_1 and x_2 direction are negligible, the streamwise and spanwise pressure gradients are assumed to be constant throughout the height of the modeled region, and are therefore determined by the LES sample location, and that the inner layer responds instantly to fluctuations in the outer layer, decoupling the timestep taken in the wall-solve from the global timestep. With the above assumptions the final form of the equations become:

u-velocity

$$\frac{1}{\Delta t}\delta u^{k+1} - \frac{1}{\rho^k}\frac{\partial}{\partial x_3}\left[\hat{\mu}^k \frac{\partial \delta u^{k+1}}{\partial x_3}\right] = \left[\frac{1}{\rho}\frac{\partial}{\partial x_3}\left(\hat{\mu}\frac{\partial u}{\partial x_3}\right)\right]^k - \frac{1}{\rho^k}\left[\sum_{j=1}^{2}\frac{\partial}{\partial x_j}(\rho u_1 u_j + p\delta_{1j})\right]^n \tag{17}$$

v-velocity

$$\frac{1}{\Delta t}\delta v^{k+1} - \frac{1}{\rho^k}\frac{\partial}{\partial x_3}\left[\hat{\mu}^k \frac{\partial \delta v^{k+1}}{\partial x_3}\right] = \left[\frac{1}{\rho}\frac{\partial}{\partial x_3}\left(\hat{\mu}\frac{\partial v}{\partial x_3}\right)\right]^k - \frac{1}{\rho^k}\left[\sum_{j=1}^{2}\frac{\partial}{\partial x_j}(\rho u_2 u_j + p\delta_{2j})\right]^n \tag{18}$$

specific energy

$$\frac{1}{\Delta t}\delta e^{k+1} - \frac{1}{\rho^k}\frac{\partial}{\partial x_3}\left[\frac{\kappa^k}{c_v}\frac{\partial \delta e^{k+1}}{\partial x_3}\right] = \left[\frac{1}{\rho}\frac{\partial}{\partial x_3}\left(u\hat{\mu}\frac{\partial u}{\partial x_3} + v\hat{\mu}\frac{\partial v}{\partial x_3} + \hat{\kappa}\frac{\partial T}{\partial x_3}\right)\right]^k - \frac{1}{\rho^k}\left[\sum_{j=1}^{2}\frac{\partial}{\partial x_j}\{(E+p)u_j\}\right]^n \tag{19}$$

SA variable

$$\mathcal{A}\delta\tilde{\nu}^{k+1} - \frac{2c_{b2}}{\sigma\rho^k}\mathcal{B}\frac{\partial}{\partial x_3}\delta\tilde{\nu}^{k+1} - \frac{1}{\sigma\rho^k}\frac{\partial}{\partial x_3}\left(\mathcal{C}\delta\tilde{\nu}^{k+1}\right) - \frac{1}{\sigma\rho^k}\frac{\partial}{\partial x_3}\left(\mathcal{D}\frac{\partial\delta\tilde{\nu}^{k+1}}{\partial x_3}\right) = \mathcal{E}\Big|^k \tag{20}$$

where the coefficients of the SA equation are:

$$\mathcal{A} = \left[\frac{1}{\Delta t} - \left(c_{b1}\tilde{S} - \frac{c_{w1}f_w}{d^2}\tilde{\nu}\right) - \frac{2c_{b2}}{\sigma\rho}\left(\tilde{\nu}\frac{\partial\sqrt{\rho}}{\partial x_3}\frac{\partial\sqrt{\rho}}{\partial x_3} + \sqrt{\rho}\frac{\partial\sqrt{\rho}}{\partial x_3}\frac{\partial\tilde{\nu}}{\partial x_3}\right)\right]^k \tag{21}$$

$$\mathcal{B} = \left(\rho\frac{\partial\tilde{\nu}}{\partial x_3} + \sqrt{\rho}\tilde{\nu}\frac{\partial\sqrt{\rho}}{\partial x_3}\right)^k \tag{22}$$

$$\mathcal{C} = \left(2\sqrt{\rho}\tilde{\nu}\frac{\partial\sqrt{\rho}}{\partial x_3} + \rho\frac{\partial\tilde{\nu}}{\partial x_3}\right)^k \tag{23}$$

$$\mathcal{D} = (\mu + \rho\tilde{\nu})^k \tag{24}$$

$$\mathcal{E} = \frac{1}{\rho^k}\left\{S_P - S_D + \frac{1}{\sigma}\left[\frac{\partial}{\partial x_3}\left(\mu\frac{\partial\tilde{\nu}}{\partial x_3}\right) + \frac{\partial}{\partial x_3}\left(\sqrt{\rho}\tilde{\nu}^2\frac{\partial\sqrt{\rho}}{\partial x_3} + \rho\tilde{\nu}\frac{\partial\tilde{\nu}}{\partial x_3}\right) + c_{b2}\left(\sqrt{\rho}\frac{\partial\tilde{\nu}}{\partial x_3} + \tilde{\nu}\frac{\partial\sqrt{\rho}}{\partial x_3}\right)^2\right]\right\}^k \tag{25}$$

Where needed, $\tilde{S}$ is limited from reaching negative values using the method suggested by Allmaras et al.[7] Equations (17) - (20) are discretized using second-order central differencing. The index n indicates data from the previous solver timestep, which his held constant while solving the wall-model. The k index represents data from previous iterations. As was done in the work by Bond and Blottner,[10] the equations are solved iteratively using an inner-loop/outer-loop construct. On the inner loop, only the variable being solved for is updated in each equation. An outer loop exists to sync the flow variable amongst the equations, and to update the density field.

III.D. Boundary Conditions

The boundary conditions for Eqs. (17) - (20) are determined by the wall-state and the LES solution at the probe location. The values on the boundary are held fixed for the wall-model calculation. Turbulent eddy viscosity is specified to be zero at the wall, however its determination at he outer boundary differs depending on which viscosity model is used. If the mixing length model is used, the value is determined by the model and updated at each iteration. If the SA-Catris model is used, the value of the SA variable on the boundary is chosen to produce the eddy-viscosity from the LES or RANS at that point, and held fixed throughout the wall model calculation.

IV. A Posteriori Evaluation

We conducted a posteriori analysis to evaluate the accuracy of the proposed wall model, and the performance of the various eddy viscosity models. For this analysis, we chose the to use the forebody data from the CUBRC LENS-II Hollow-Cylinder Flare (HCF) and Large Cone Flare (LCF) experiments from the shock wave/turbulent boundary layer study presented at AIAA Aviation 2014.[14] The HCF forebody is a hollow cylinder with an outer diameter of 0.496 meters and a length of 2.474 meters. The LCF forebody is a 7-degree cone with an axis length of 2.35 meters. The test conditions used for each geometry are given in table 2.

	HCF run 16	LCF run 14
Mach	4.97	7.14
Re_L	8.54×10^7	5.27×10^7
T_w/T_0	0.25	0.52

Table 2. Test conditions for CUBRC LENS-II HCF and LCF experiments.[14]

We chose these conditions due to the high Mach number, cold-wall isothermal conditions, and large extent of flow over the test articles where inertial effects and pressure gradients are negligible. Simulations were conducted in US3D using modified Steger-Warming flux vector splitting[15] with second-order MUSCL on density, velocities, turbulence variable and pressure, gradients evaluated by weighted least-squares, molecular viscosity determined by Sutherland's formula, and turbulent viscosity from the SA-Catris Model.[13] Time integration was accomplished with the DPLR[16] method to drive the flow to steady-state. The 2-D axisymmetric grids were resolved to the wall with a $y^+ \ll 1$. Data extraction locations .5, 1.1, and 1.5 meters from the leading edge were chosen to minimize the influence from both the leading edge of the geometry and downstream shock-shock interaction. Probe data were extracted from the converged US3D solutions at various heights in the boundary layer and used as boundary values for evaluation of the wall model. The heat flux and wall-shear determined by the US3D simulations are given in table 3.

	HCF Run 16			LCF Run 14		
x [m]	0.5	1.1	1.5	0.5	1.1	1.5
τ_w [Pa]	309.18	276.15	263.58	86.56	76.84	73.31
q_w [W/cm^2]	21.11	18.83	17.96	2.23	1.99	1.90

Table 3. US3D wall shear and heat flux.

Both of these test conditions are axisymmetric with no surface curvature in the streamwise direction in the area of interest. To capitalize on this fact and simplify the model formulation, the wall-tangent flux derivatives in Eq. (16) are neglected in the current implementation of the wall-model. This results in a purely 1-D model involving only diffusive terms, as is common practice in wall modeling. This assumption will result in error for regions of flow where pressure gradients and inertial terms are non-negligible.

IV.A. Baseline Solutions

IV.A.1. Hollow-Cylinder Flare

Figure 2 shows the reference boundary layer profile computed by US3D at the 1.1 meter station in wall units. Notable features include a peak in the SA variable at a distance of 2800 wall units above the surface, and a peak temperature overshoot at 28 wall units. There is a very strong temperature gradient in the inner portion of the boundary layer to recover the cold-wall temperature from the peak temperature location. Associated with the temperature variation are strong density gradients throughout the boundary layer which peaks below 30 wall units. The same features are present at the other stations at different different values of y^+.

IV.A.2. Large Cone Flare

Figure 3 shows the reference boundary layer profile computed by US3D at the 1.1 meter station in wall units. The boundary layer at this station for the LCF case is only 1000 wall units tall. The SA variable peaks at approximately 400 wall units, while the temperature peaks very close to the wall at six wall units.

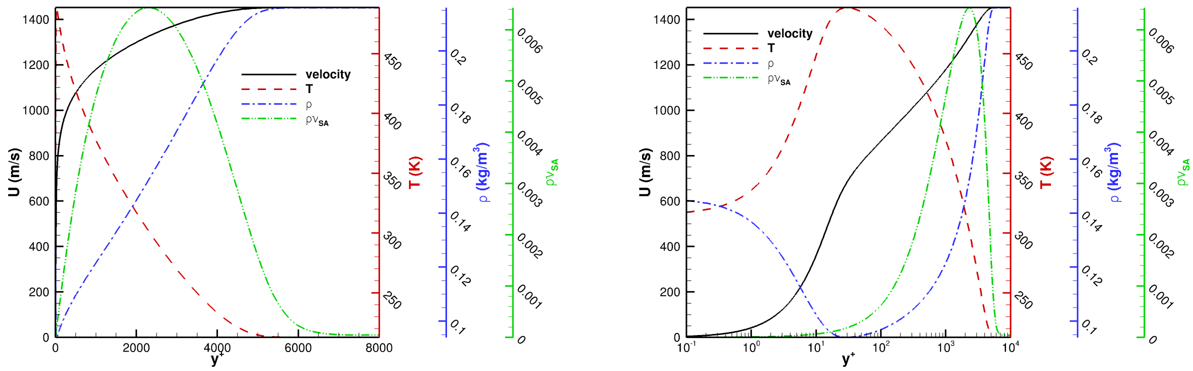

(a) wall-unit

(b) log wall-unit

Figure 2. US3D HCF boundary layer profile x=1.1m

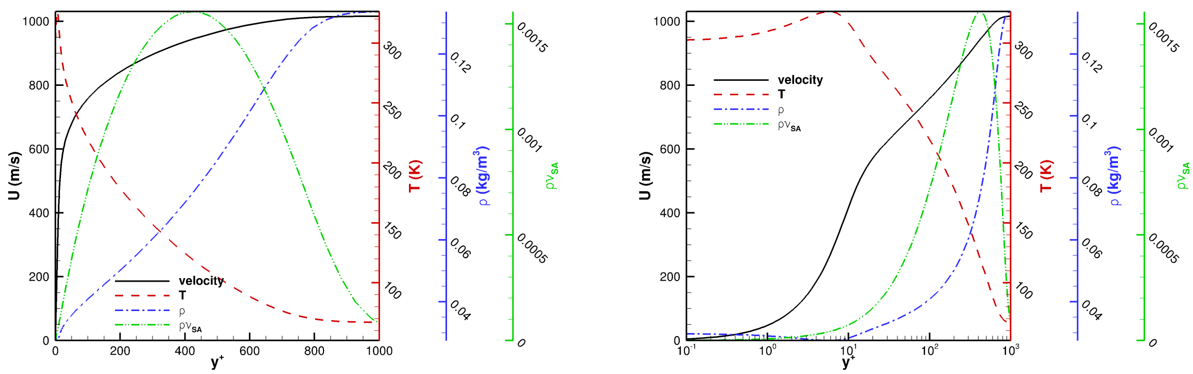

(a) wall-unit

(b) log wall-unit

Figure 3. US3D LCF boundary layer profile x=1.1m

At this station the wall temperature is very close to the peak temperature overshoot, leading to very mild temperature and density gradients in the viscous sub-layer of the boundary layer. The boundary layer profiles at the $x = 0.5$ m and $x = 1.5$ m station are qualitatively similar to the profile presented in Fig. 3 with the predominate difference being the total height of the boundary layer.

IV.B. Model Performance

To evaluate the various formulations of the proposed wall model, data were sampled from the baseline boundary layer at specific heights in the boundary layer. Those data were used as boundary conditions for the wall model's ODE solve. The models were run independently of the solution that generated the baseline profiles. For both proposed eddy viscosity formulations, a single iteration of the inner loop was sufficient to stabilize the outer loop to convergence. In all cases the models converged to machine zero in negligible computational time.

The following model factors were examined:

- The impact of choice of eddy viscosity model
- The impact of probe height for the wall-model

To evaluate the above factors, boundary layer profiles computed by the wall model were compared to those from the reference solution. Additionally, we compared predictions of wall shear and heat flux from the wall models to the baseline solutions.

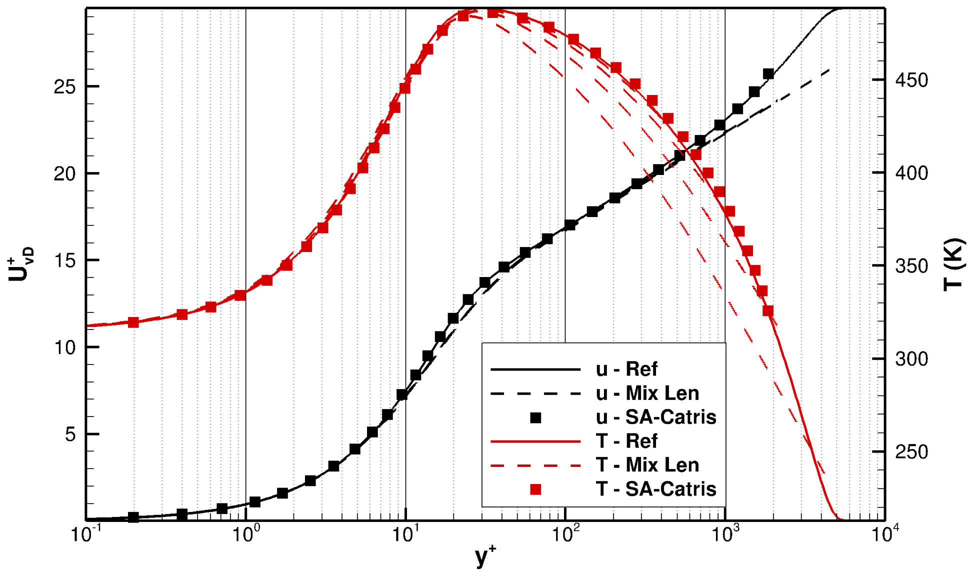

Figure 4. Velocity and temperature profiles for HCF at x = 1.1m

IV.B.1. Hollow-Cylinder Flare

Van Driest-transformed Velocity and temperature profiles computed by both eddy viscosity models with data extracted at various probe locations at the $x = 1.1$ meter station of the HCF are shown in Fig. 4. For probe locations placed more than 1000 wall unites from the wall the mixing length model boundary layer profiles deviate significantly from the reference boundary layer. Use of the SA-Catris model to determine turbulent eddy viscosity significantly improves the wall model's approximation of the boundary layer profile.

Figures 5 through 7 show the wall shear and heat flux predicted by the two eddy-viscosity models for varying probe locations. These values are normalized by the quantity produced by the reference solution. The mixing length model significantly overpredicts both wall shear and het transfer for probe location at or beyond 1000 wall units at all stations. The SA-Catris model shows asymptotic convergence at all stations as the probe is brought closer to the wall. Compared to the predictions made by the mixing length-based model, the SA-Catris model more accurately determines wall shear and heat transfer at every station and at each probe location.

The wall shear and heat-flux calculations produced by the mixing length model are accurate so long as the probe is placed near the inner region of the boundary layer where viscous dissipation dominates the solution. Probes placed further into the log region of the boundary led to rapidly diverging predictions of both wall shear and heat flux. For cases where the probe was placed further into the log-layer, not only is density variation be a factor, but so is non-linear variation of the production of turbulent kinetic energy, and by extension turbulent eddy viscosity. While most CFD practitioners refrain from using mixing length models outside of the inner-layer of a boundary layer, the employment of Kawai and Larsson[3] like probe placement methods will result in interface points being placed further into a boundary layer than has traditionally been accepted practice. This occurrence should be accounted for when choosing a turbulence modeling strategy.

IV.B.2. Large Cone Flare

Van Driest-transformed Velocity and temperature profiles computed by both eddy viscosity models with data extracted at various probe locations at the $x = 1.1$ meter station of the LCF are shown in Fig. 8. As was seen in the HCF case, for probe locations placed in the log-law region the mixing length model boundary layer profiles deviate significantly from the reference boundary layer. Use of the SA-Catris model to determine turbulent eddy viscosity significantly improves the wall model's approximation of the boundary layer temperature profile, however it does not improve the van Driest velocity profile compared to the mixing

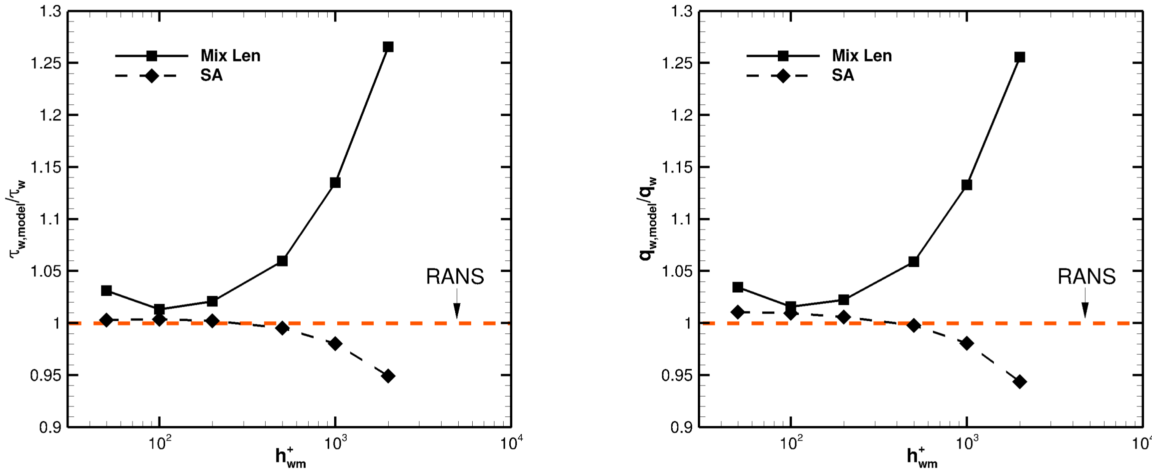

(a) wall-shear (b) heat-transfer

Figure 5. Wall fluxes determined by two eddy-viscosity models on HCF at x=0.5m with varying probe heights.

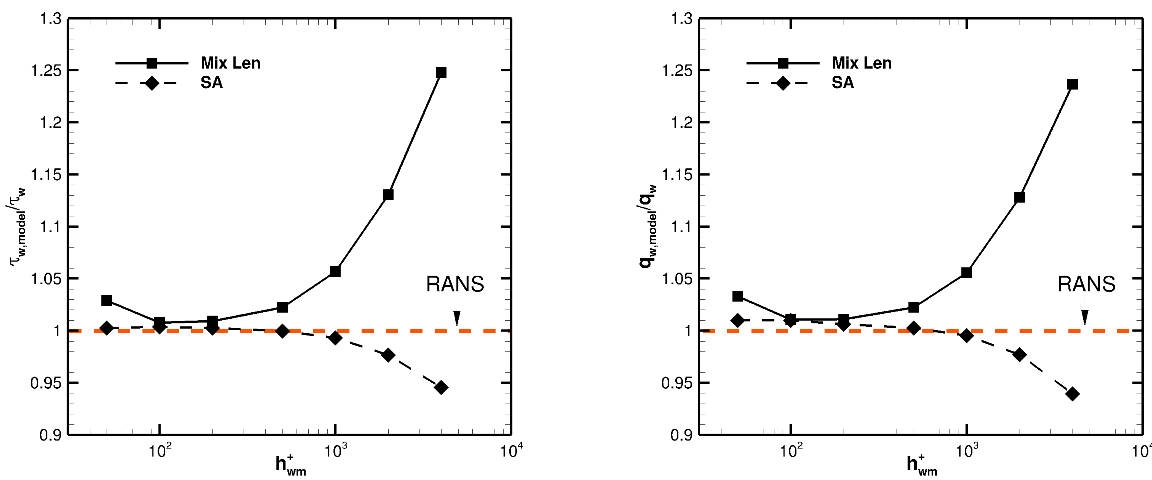

(a) wall-shear (b) heat-transfer

Figure 6. Wall fluxes determined by two eddy-viscosity models on HCF at x=1.1m with varying probe heights.

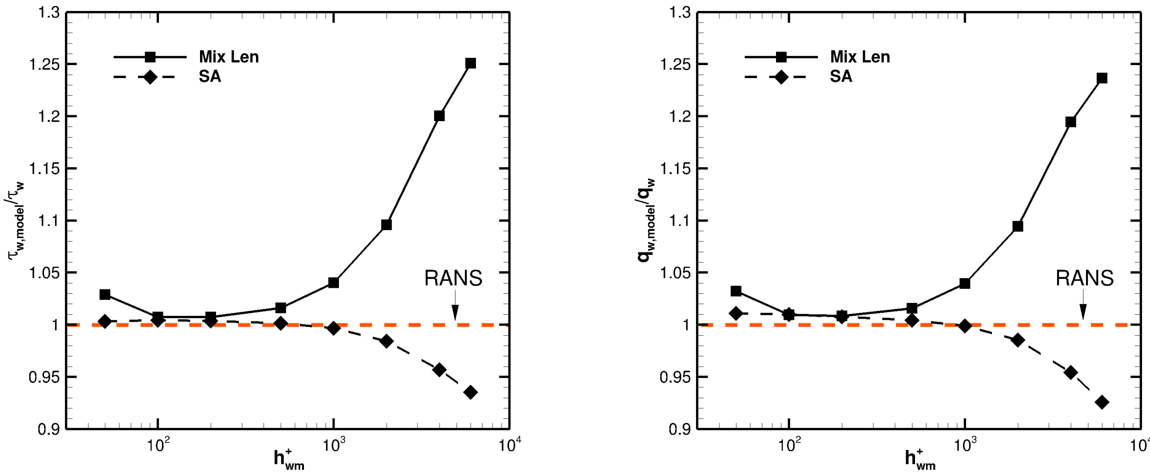

(a) wall-shear

(b) heat-transfer

Figure 7. Wall fluxes determined by two eddy-viscosity models on HCF at x=1.5m with varying probe heights.

length model.

Figures 9 through 11 show the predicted wall shear and heat flux for LCF geometry using both eddy viscosity models at varying probe locations. The predicted quantities are normalized by the values produced by the reference solution. Both models converge towards similar values of wall shear and heat flux as the probe is brought closer to the surface, however this value is significantly less than the resolved RANS result. The error associated with each eddy viscosity model at the closest probe location ($y^+ = 50$) is presented in table 4.

	Mixing Length			SA-Catris		
x [m]	0.5	1.1	1.5	0.5	1.1	1.5
τ_w [%]	-6.8	-10.7	-11.7	-9.3	-10.4	-10.8
q_w [%]	-5.9	-10.6	-11.5	-9.7	-10.9	-11.2

Table 4. Error in predicted wall quantities for LCF at a probe $y^+ = 50$

The fact that both turbulence models are converging to lower values of wall shear and heat flux than the RANS solution indicate that the error lies in a discrepancy between the wall model formulation and the physics of the LCF test case. Compared to the the HCF test case, the LCF has a much smaller radius of curvature in rotational symmetry. Additionally, the LCF flowfield has a strong attached shock that results in non-negligible pressure variation throughout the entire post-shock region, including the boundary layer. Additionally, an entropy layer is present due to the shock. The particular implementation of Eq. (16) being tested does not account for inertial effects, pressure gradients, or axisymmetry.

V. Conclusion

We presented the derivation of a turbulence wall model suitable for high Reynolds number cold-wall flows involving shock turbulent boundary layer interactions. The equations were presented in a form that allows for rapid convergence of the model despite strong density and temperature gradients at the wall.

A posteriori analysis was conducted simulations of the CUBRC LENS-II hollow cylinder flare and large cone flare to validate the wall model and evaluate the performance of two eddy viscosity models. We considered determining eddy viscosity via a mixing length model and the Catris-Aupoix formulation of the Spalart-Allmaras one-equation turbulence model.

For the HCF case, both eddy viscosity models produced accurate values of wall shear and heat flux for probe locations placed near the wall. As the probe moved away from the wall into the log-layer, the wall

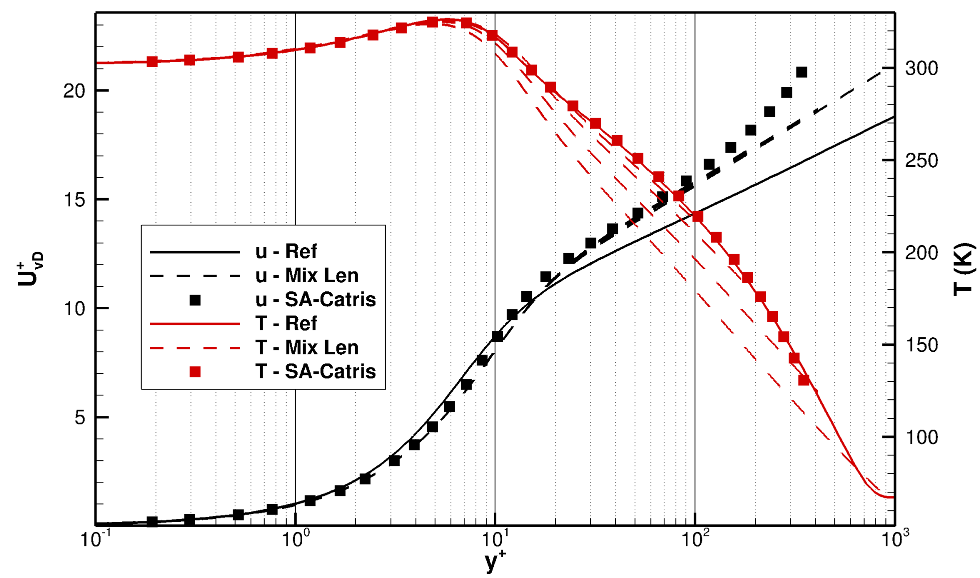

Figure 8. Velocity and temperature profiles for LCF at x = 1.1m

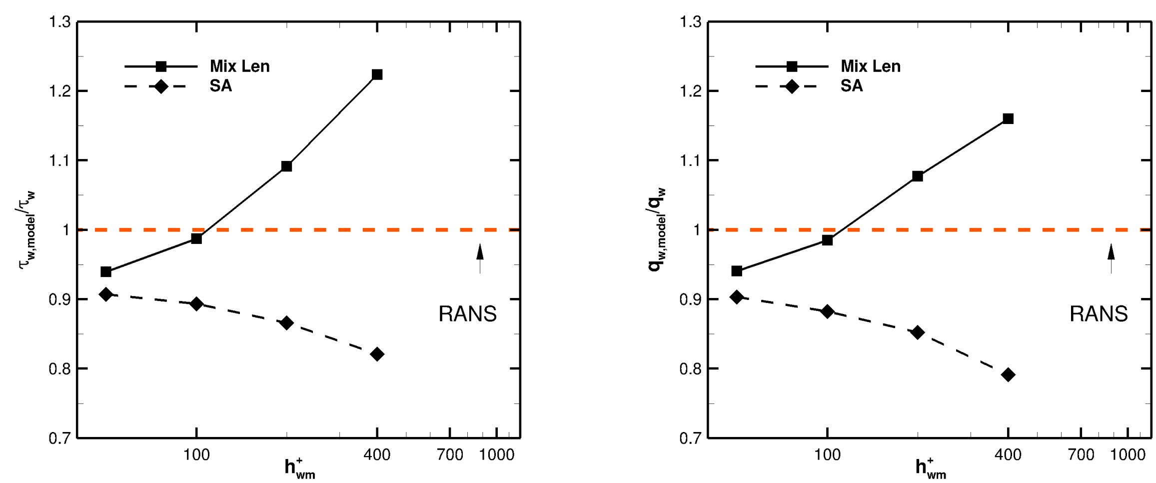

(a) wall-shear

(b) heat-transfer

Figure 9. Wall fluxes determined by two eddy-viscosity models on LCF at x=0.5m with varying probe heights.

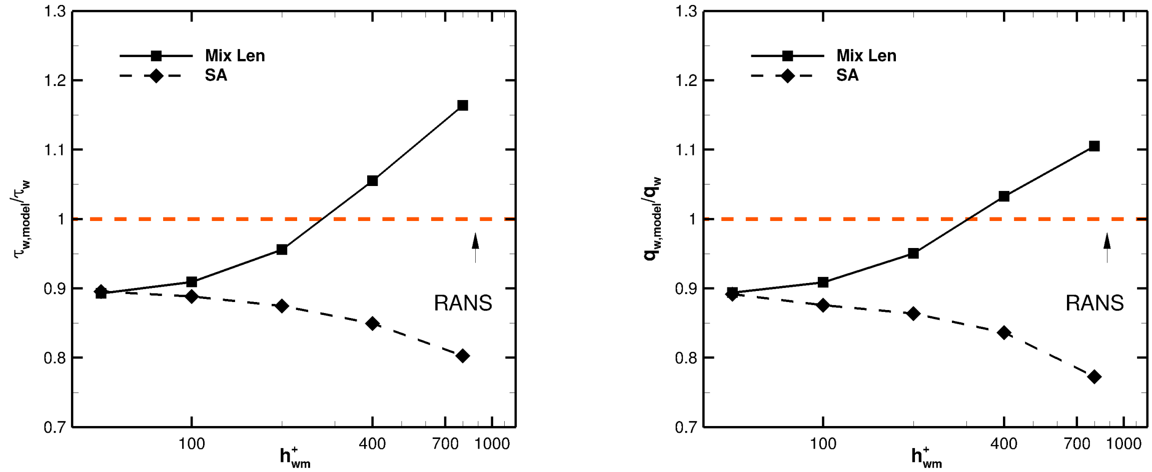

(a) wall-shear (b) heat-transfer

Figure 10. Wall fluxes determined by two eddy-viscosity models on LCF at x=1.1m with varying probe heights.

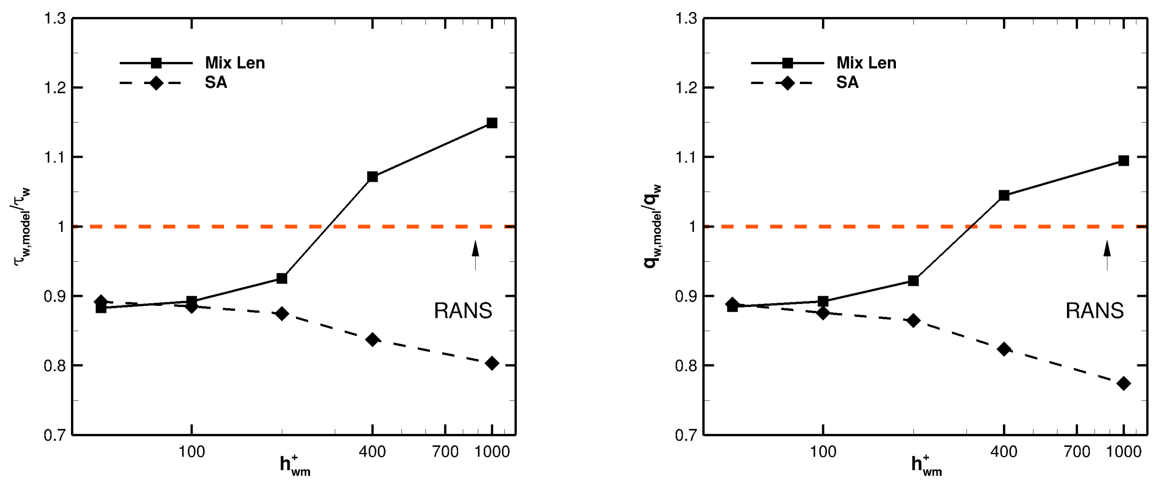

(a) wall-shear (b) heat-transfer

Figure 11. Wall fluxes determined by two eddy-viscosity models on LCF at x=1.5m with varying probe heights.

model solution produced using the mixing length model departed rapidly from the reference solution while the solution produced by SA-Catris model remained accurate. It is important to keep this limitation of the mixing length model in mind when choosing modeling strategies for very coarse grids, or models with probe placement several cells off the wall.

For the LCF case, both eddy viscosity models produced wall shear and heat flux values that did not agree with the reference simulation, however they agreed with each other as the probe was moved closer to the wall. This systemic error may be due to the fact that the model used to evaluate this case neglected the inertial inertial and pressure gradient terms in the model's formulation. This work suggests that equilibrium wall models may omit terms necessary to model cold-wall boundary layers on cones.

Acknowledgements

The authors would like to acknowledge the efforts of all of the institutions supporting the Air Force Research Laboratory's Collaborative Center for Aeronautical Sciences, as well as the Boeing Corporation for their support of this work.

References

[1]Choi, H. and Moin, P., "Grid-point requirements for large eddy simulation: Chapman's estimates revisited," *Physics of Fluids (1994-present)*, Vol. 24, No. 1, 2012.

[2]Chapman, D. R., "Computational aerodynamics development and outlook," *AIAA journal*, Vol. 17, No. 12, 1979, pp. 1293–1313.

[3]Kawai, S. and Larsson, J., "Wall-modeling in large eddy simulation: Length scales, grid resolution, and accuracy," *Physics of Fluids (1994-present)*, Vol. 24, No. 1, 2012, pp. 015105.

[4]Dawson, D. M., Bodart, J., and Lele, S. K., "Assessment of Wall-modeled Large Eddy Simulation For Supersonic Compression Ramp Flows," AIAA/ASME/SAE/ASEE Joint Propulsion Conference, 2013.

[5]Nichols, R. H. and Nelson, C., "Wall function boundary conditions including heat transfer and compressibility," *AIAA journal*, Vol. 42, No. 6, 2004, pp. 1107–1114.

[6]Vane, Z. P. and Lele, S. K., "Simulations of a Normal Shock Train in a Constant Area Duct Using Wall-Modeled LES," *43rd Fluid Dynamics Conference*, American Institute of Aeronautics and Astronautics, 2013.

[7]Allmaras, S. R., Johnson, F. T., and Spalart, P. R., "Modifications and clarifications for the implementation of the spalart-allmaras turbulence model," *Seventh International Conference on Computational Fluid Dynamics (ICCFD7)*, 2012, pp. 1–11.

[8]Nompelis, I., Drayna, T., and Candler, G., "A Parallel Unstructured Implicit Solver for Hypersonic Reacting Flow Simulation," *17th AIAA Computational Fluid Dynamics Conference*, 2005.

[9]Hickel, S., Touber, E., Bodart, J., and Larsson, J., "A parametrized non-equilibrium wall-model for large-eddy simulations," *Proceedings of the Summer Program*, Center for Turbulence Research, Stanford University, 2012, p. 127.

[10]Bond, R. and Blottner, F. G., "Derivation, implementation, and initial testing of a compressible wall-layer model," *International Journal for Numerical Methods in Fluids*, Vol. 66, No. 9, 2011, pp. 1183–1206.

[11]Kawai, S. and Larsson, J., "A Non-Equilibrium Wall-Model for LES of Shock/Boundary Layer Interaction at High Reynolds Number," *42nd AIAA Fluid Dynamics Conference and Exhibit*, American Institute of Aeronautics and Astronautics, 2012.

[12]Vane, Z. P., Bermejo-Moreno, I., and Lele, S. K., "Wall-Modeled Large-Eddy Simulations of a Supersonic Turbulent Flow in a Square Duct," *44th AIAA Fluid Dynamics Conference*, American Institute of Aeronautics and Astronautics, 2014.

[13]Catris, S. and Aupoix, B., "Density corrections for turbulence models," *Aerospace Science and Technology*, Vol. 4, No. 1, 2000, pp. 1 – 11.

[14]Holden, M. S., Wadhams, T. P., and MacLean, M., "Shock Wave/Turbulent Boundary Layer (SWTBL) Study Presented At AIAA Aviation 2014," `http://www.cubrc.org/index.php?option=com_content&view=article&id=121&Itemid=64`.

[15]Candler, G. V., Subbareddy, P. K., and Nompelis, I., "CFD Methods for Hypersonic Flows and Aerothermodynamics," *Progress in Astronautics and Aeronautics*, 2015, pp. 203–237.

[16]Wright, M. J., Candler, G. V., and Bose, D., "Data-Parallel Line-Relaxation Method for the Navier-Stokes Equations," *AIAA Journal*, Vol. 36, No. 9, September 1998, pp. 1603–1609.